Journal of *Marine Science and Engineering*

MDPI

Article

Numerical Research on Hull–Propeller–Rudder–Ice Interaction of Full-Scale Polar Transport Ship in Brash Ice Channel

Jinlong Zhang [1], Jianing Zhang [1,*], Lei Zhang [1], Weimin Chen [2,3] and Qingshan Zhang [2,3]

[1] School of Naval Architecture and Ocean Engineering, Dalian Maritime University, Dalian 116026, China; zhangjinlongchn@163.com (J.Z.); zhanglei2020@dlmu.edu.cn (L.Z.)
[2] State Key Laboratory of Navigation and Safety Technology, Shanghai Ship and Shipping Research Institute Co., Ltd., Shanghai 200135, China; chen.weimin@coscoshipping.com (W.C.); zhang.qingshan@coscoshipping.com (Q.Z.)
[3] Key Laboratory of Marine Technology, Shanghai Ship and Shipping Research Institute Co., Ltd., Shanghai 200135, China
* Correspondence: zhangjianing@dlmu.edu.cn

Abstract: A strong nonlinear ice load has a significant impact on the resistance and power demand of polar transport ships under different drafts in brash ice channels. In this study, the CFD-DEM coupling method is used to investigate the self-propulsion performance of a full-scale polar transport ship in brash ice channels. The interactions between the full-scale polar transport ship, propeller, rudder, and brash ice are effectively simulated. First, the hydrodynamic performance of an open-water propeller is tested, and it is found that the numerical errors of efficiency and the experimental result are less than 8%. Then, the ice resistance, total thrust, effective power, delivered power, and propulsive efficiency of the polar transport ship under different draft conditions are studied, and the results are in good agreement with those of the self-propulsion model tests in the brash ice channel. Through a numerical simulation of self-propulsion in the brash ice channel, self-propulsion points under different drafts and brash ice thicknesses are obtained. It is found that the propeller rotation speed is closely related to the draft depth. Finally, experiments and numerical simulations of the total ice resistance are carried out under different brash ice thicknesses, and the results are consistent with those of the empirical formulas. The accuracy of the three empirical formulas under different drafts is compared. This research work determines the resistance, power demand, and propulsive efficiency of a polar transport ship under given ice conditions and speeds, as well as the self-propulsion points under different ice thicknesses. It is of great significance for the control of ships in polar navigation.

Keywords: CFD-DEM model; ice resistance; propeller rotation speed; self-propulsion; model test; delivered power forecast

check for updates

Academic Editor: Weicheng Cui

Received: 19 December 2024
Revised: 10 January 2025
Accepted: 12 January 2025
Published: 15 January 2025

Citation: Zhang, J.; Zhang, J.; Zhang, L.; Chen, W.; Zhang, Q. Numerical Research on Hull–Propeller–Rudder–Ice Interaction of Full-Scale Polar Transport Ship in Brash Ice Channel. *J. Mar. Sci. Eng.* **2025**, *13*, 145. https://doi.org/10.3390/jmse13010145

Copyright: © 2025 by the authors. Licensee MDPI, Basel, Switzerland. This article is an open access article distributed under the terms and conditions of the Creative Commons Attribution (CC BY) license (https://creativecommons.org/licenses/by/4.0/).

1. Introduction

With global climate change, the extent, thickness, and concentration of ice have generally decreased. In polar environments, level ice breaks down into floating brash ice, which takes on various shapes under the combined action of wind, waves, and currents. There are increasingly more brash ice areas in polar regions. Therefore, studying the load characteristics of ships in brash ice channels is crucial for guiding ship design in polar ice regions. The size of the ice load, main engine power, and sea ice affect the structural strength of ships in polar ice regions. The research methods for ship ice resistance mainly include the empirical formula method, model test method, and numerical simulation method. Since the cost of the model test method is relatively high, constructing an ice tank is an efficient research method for the numerical

simulation of ships in ice areas. Therefore, the study of the load characteristics of polar transport ships is a more urgent research topic in the shipping industry.

Shimanskiĭ [1] investigated the icebreaking resistance of icebreaking ships through the application of a semi-empirical formula. The study suggests that the parameters associated with the semi-empirical formula should be determined based on actual ship data. Kashteljan [2] divided the empirical prediction formula into three parts: icebreaking resistance, immersion resistance, and rotational resistance of crushed ice pieces. Edwards et al. [3] made modifications to the empirical formula and assessed the ice resistance for the icebreaker Mackinaw, and the results align well with the full-scale data.

Zhou et al. [4] conducted model experiments on the Uikku ship model. By changing the ice thickness, drift angle, and velocity, the ice load was obtained from the model experiment. Zong et al. [5] conducted ship model towing experiments using artificial ice floes made of PP material. After varying the size, shape, and concentrations of the simulated ice, the results were similar to those of other researchers' experiments. Huang et al. [6] conducted model tests on icebreakers in both normal-level ice and ice covered with snow. Compared with the Lindqvist method, the snow increased the ice resistance on the breaking and immersion. The self-propulsion model test of ships in ice areas can determine the ship's resistance, power demand, and propulsive efficiency under a given ice condition and speed and be used to observe the contact between broken ice and hull. ITTC provides ice model tests and ice resistance descriptions and guidelines [7,8].

Cundall et al. [9] proposed the discrete element method based on the principles of molecular dynamics. Vu et al. [10] proposed a three-dimensional discrete model for dry granular flow using ellipsoidal particles and conducted numerical simulations. As the shapes of discrete elements grow more intricate, inter-unit computations also become more difficult. Løset et al. [11] simulated the interactions between ship and ice, providing initial evidence for the validity of the DEM method. Squire et al. [12] distinguished two main types of sea ice, continuous ice typically found in the central Arctic and ice in marginal areas near open water, and considered the interaction between waves and sea ice, utilizing complex mathematical models. Su et al. [13] presented a numerical approach for simulating ship maneuvers in level ice and solved the equations of motion for surge, sway, and yaw in three degrees of freedom for rigid body dynamics. Kim et al. [14] developed an ice resistance estimation system and compared the calculated results for an oil tanker with model test results, and the error was below 15%, indicating good accuracy of the estimation system.

Zhang et al. [15] performed numerical calculations of ice loads on a full-scale AFRAMAX oil tanker. They discussed the impact of three contact models and ice particle shapes on ice loads, and the numerical simulation error was within a certain range. Li et al. [16] used Green's function and boundary integral equation method to study the hydrodynamic problems of the interaction between waves and ships near semi-infinite ice layers and studied the numerical results of the added mass, damping coefficient, and wave excitation force of the ship at different positions, ice thicknesses, and incident wave angles. Luo et al. [17] used a DEM-coupled approach to investigate the resistance in fragmented ice channels and studied the impact of the shape of ice particles on ice load characteristics. Liu and Ji [18] investigated the sphere-based discrete element method, SDEM, and DPDEM, and SDEM performed well in simulating sea ice fragmentation. Both SDEM and DPDEM obtained similar ice resistance, while the ice load calculated by the Lindqvist formula was higher. Li et al. [19] investigated ship performance in narrow ice channels. The simulation results demonstrated that the method accurately calculates the variation of ship resistance with channel width. Islam et al. [20] conducted an extensive literature review and summarized research methods for ship–ice interactions, such as FEM, DEM, PIC, and SPH, briefly discussing their advantages and limitations. Wang et al. [21] used LS-DYNA (2006) to analyze

the effects of speed and concentration on ice loads. Kim et al. [22] simulated the effects of different sizes, concentrations, thicknesses, and floe shapes on ice loads and found that the numerical outcomes were in good accordance with the experimental results. Yang et al. [23] used the Lagrangian–Eulerian formulation to estimate the ice resistance of ships in floating ice. They used an ice field generation algorithm to create a random distribution of floating ice. Zhang et al. [24] established a CFD model for the free-running maneuvering of a trimaran, incorporating the region motion method. Compared to model tests, the MMG method was found to be more effective. Zou et al. [25] used the DEM method and took a Panama bulk carrier as the research object to study the effects of speed, the thickness of broken ice on ice resistance, and a ship's force distribution during ship–ice collision. Xie et al. [26] used the DEM method to study the self-propulsion performance of ships and obtained the collision force generated by ship–ice interactions and propeller–ice collisions.

In previous studies, most scholars used the virtual disk method instead of a real propeller to investigate the self-propulsion characteristics of ships in open water. At present, in research on ships in brash ice regions, scholars are paying more attention to ship ice resistance characteristics, while few scholars pay attention to the relationship between real propeller rotation, full-scale ships, the rudder, and brash ice. In this study, polar transport ships are taken as the research object, and a full-scale ship, propeller, rudder, and ice coupling numerical model is constructed. A self-propulsion numerical simulation of the full-scale polar transport ship is carried out under scantling and design draft conditions.

2. Numerical Method

2.1. Governing Equations of the Incompressible Fluid

The basics for all CFD simulations are set using governing equations, i.e., the continuity and Navier–Stokes equations. In simulations, the flow is assumed to be incompressible, i.e., the density and viscosity are constant.

$$\frac{\partial_{ui}}{\partial_{xi}} = 0 \tag{1}$$

$$\frac{\partial_{ui}}{\partial_t} + u_j \frac{\partial_{ui}}{\partial_{xj}} = -\frac{1}{\rho}\frac{\partial_p}{\partial_{xi}} + S_j + \mu \frac{\partial^2 u_i}{\partial_{x_j}\partial_{x_j}} \tag{2}$$

The continuity equation has to be time-averaged. ρ is the fluid density, and t is the time. P is the time mean of the pressure, S_j is the generalized source term of the momentum equation, and μ is the dynamic viscosity coefficient.

The wall function method is used to generate near-wall phenomena more efficiently, where wall functions are selected based on mesh. This study adopts a free surface viscous flow simulation, utilizing the VOF method to capture the interface and adopting VOF wave damping to reduce boundary emissions from the simulation domain.

2.2. The Motion Equations of Ice Particles

The discrete element method, which can accurately simulate the interactions between solid particles, is used to model ice particles. DEM computation is based on an iterative calculation with small time steps in which the position and contact force of the discrete elements are updated after each iteration. In STAR-CCM+ (2019), the definition of translation conservation is as follows [27] (Siemens PLM Software, Plano, TX, USA, 2019):

$$m_p \frac{d_{v_p}}{dt} = F_s + F_b \tag{3}$$

$$I_p \frac{d_{w_p}}{dt} = M_b + M_c \tag{4}$$

where m_p and I_p represent the mass and inertia moment of the ice particle, respectively; v_p and ω_p represent the velocity and angular velocity of the ice particle, respectively. F_s is the resultant of the forces that act on the surface of the particle, F_b is the resultant of the body forces, M_b represents the torque on the particle, and M_c is the total moment from contact forces.

2.3. DEM Contact Models

In numerical simulations, different contact models can be used to simulate collisions between particles and walls. Considering computational efficiency, this study adopts a linear spring contact model, which is an elastic contact model that assumes that the particles in the collision are connected by linear springs in both normal and tangential directions. The model is used to represent the relationship between displacement and force. Figure 1. presents the contact force model, which allows normal and tangential spring stiffnesses to be used.

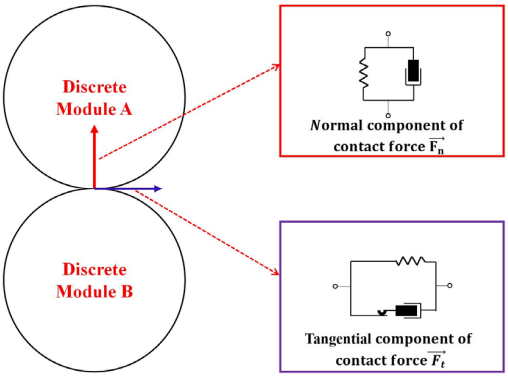


Figure 1. Discrete element contact force model. (Siemens PLM Software, 2019).

The forces between two spheres, A and B, are defined as follows in STAR-CCM+:

$$F_{contact} = F_n n + F_t t \tag{5}$$

The normal force is as follows:

$$F_n = -k_n d_n - N_n v_n \tag{6}$$

The tangential force is as follows:

$$F_t = \begin{cases} -K_t d_t - N_t v_t & ,\text{if} \left|K_t d_t\right| \leq \left|K_n d_n\right| C_{fs} \\ \frac{\left|K_n d_n\right| C_{fs} d_t}{|d_t|} & ,\text{if} \left|K_t d_t\right| > \left|K_n d_n\right| C_{fs} \end{cases} \tag{7}$$

where F_n and F_t are the magnitudes of the normal and tangential components, respectively. K_n is the normal spring stiffness, and K_t is the tangential spring stiffness. N_n is the is the normal damping, and N_t is the tangential damping. d_n is the overlap in the normal direction, and d_t is the overlap in the tangential direction. v_n is a normal component of relative sphere surface velocity at the contact point, v_t is the tangential component of relative sphere surface velocity at the contact point, and C_{fs} represents the friction coefficient.

2.4. Modeling of DEM Brash Ice Particles

In HSVA ice tests, after manually creating a brash ice channel, the shape of the brash ice is relatively uniform and maintains a certain pattern. In order to more realistically represent the brash ice channel, it is necessary to stir the broken ice evenly to make it more uniform. Due to the diverse shapes of the brash ice particles and the complexity of their position, shape, and distribution in numerical simulation, this paper establishes a

Lagrangian multiphase model. Four different thickness conditions of square ice particles were established, with the ice thickness divided into target brash ice thickness (ice class rules) and actual brash ice thickness. In this study, a component surface sprayer was used to spray the constructed ice particles into the computational domain. In numerical simulation, the density of the ice was 917 kg/m^3, the Young's modulus of the ice was 9 Gpa, and the Poisson's ratio was 0.3. Under different actual ice thickness conditions, the total resistance, total thrust, power, and propulsion efficiency of the ship were compared under a target friction coefficient of 0.1, and the magnitude and variation of these values were investigated in numerical simulation. Figure 2 shows the obtained broken ice particles.

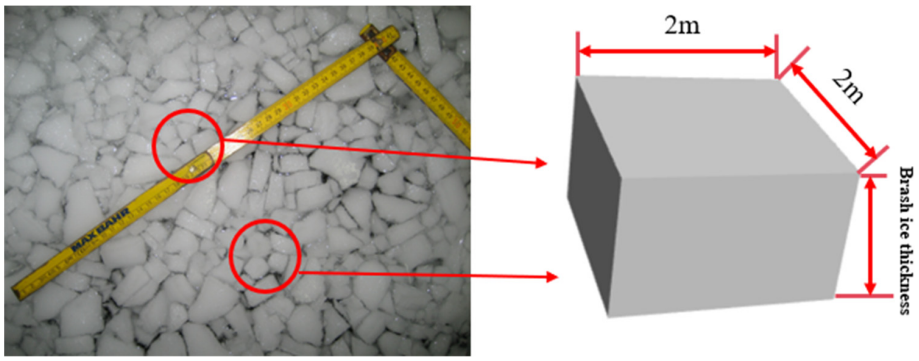


Figure 2. Ice particles in brash channel.

3. Ice Tank Test of the Model Ship

3.1. Description of Model

To investigate the interaction between the ship, propeller, rudder, and ice, the model experiment process in the HSVA was introduced. The total resistance, required total thrust, required power, and propulsive efficiency in a brash ice channel were obtained through the model test.

A polar transport ship model, with a scaling factor of 29.508, was used [28]. The ship model was equipped with a propeller and a rudder. The model was tested for the upper ice waterline (UIWL) and the lower ice waterline (LIWL). The tests were performed as towed propulsion tests at different brash ice thicknesses, which were similar to the ice thickness stipulated in the guidelines for Ice Class 1A. The experiment in the brash ice channel involved a towed propulsion test. The hull data of the ship and the main dimensions of the propeller are shown in Tables 1 and 2, respectively, and Figure 3 displays photographs of the ship model from different perspectives. The hull was treated as a rigid body, and the propeller was made of brass alloy. Deformations of the hull and propeller were not considered.

Table 1. The principal hull data of the ship model 5574-00000.

Principal Hull Data	Abbreviation	Full Scale	Model Scale
Scaling factor	λ	1	29.508
Length between perpendiculars	L_{pp} (m)	223.400	7.571
Length at upper ice waterline	L_{UIWL} (m)	226.800	7.686
Length at lower ice waterline	L_{LIWL} (m)	216.690	7.343
Breadth molded at DWL	B_{DWL} (m)	32.260	1.093
Upper ice waterline	TF_{UIWL} (m)	13.300	0.451
	TA_{UIWL} (m)	13.300	0.451
Lower ice waterline	TF_{LIWL} (m)	5.100	0.173
	TA_{LIWL} (m)	8.300	0.281

Table 2. The main dimensions of propeller.

Propeller Data	Abbreviation	Full Scale	Model Scale
Scaling factor	λ	1	29.508
Number of blades	Z	4	4
Propeller diameter	D (m)	7.200	0.244
Hub diameter	D_H	1.081	0.037

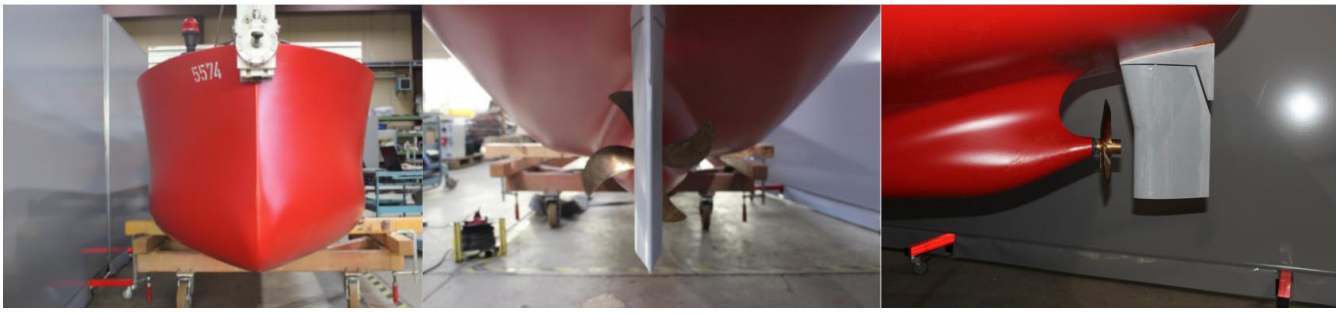
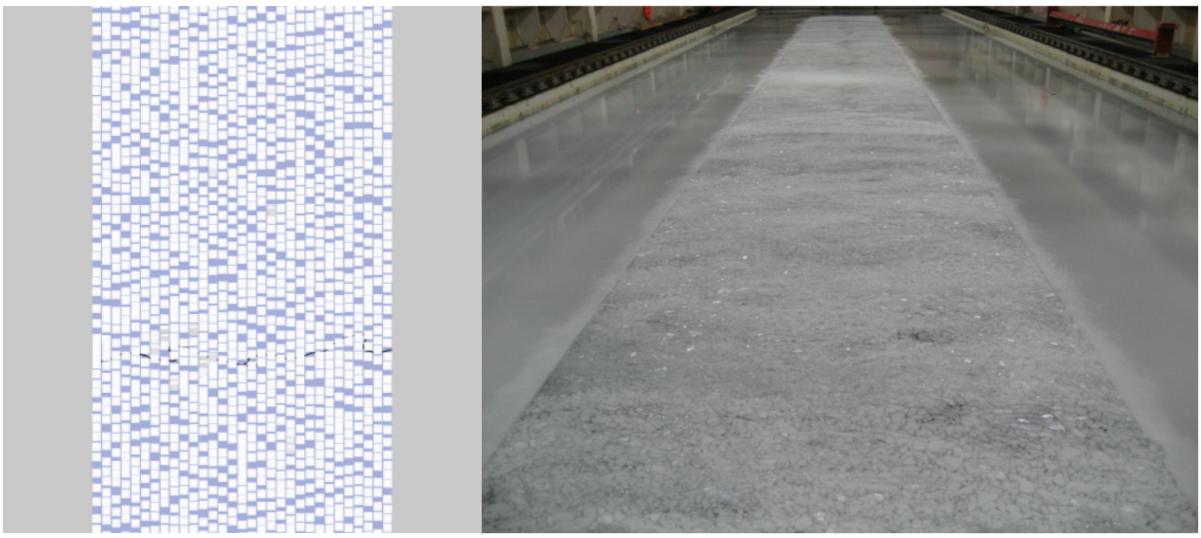


Figure 3. The ship model of 5574-00000.

3.2. Preparation of Brash Ice Channel

Due to the time-consuming and technically complex process of preparing a brash ice channel in an ice tank, testing techniques in an ice tank are significantly more complex than those employed in open-water model ship testing. In the process of creating a brash ice channel, it is necessary to prepare a sufficiently thick layer of ice cover. Then, two ice knives in an auxiliary carriage are used to accurately cut out a pen of a brash ice channel, creating a channel approximately twice the width of the ship. Careful and uniform mixing of the broken ice blocks inside the channel results in the most realistic brash ice channel. In order to obtain an ice channel with the desired brash ice thickness, it is necessary to compact the ice material in the channel. As the channel shortens due to compaction, level ice from the channel's forward side is broken up and refilled into the remaining ice-free section. The preparation of the brash ice channel for testing is shown in Figure 4.



(**a**) (**b**)

Figure 4. The preparation of brash ice channel. (**a**) The numerical brash ice channel; (**b**) brash ice channel prepared for the test run.

3.3. Model Tests in Brash Ice Channel

Bollard pull and overload tests in open water were performed on the upper ice waterline (UIWL) as well as on the lower ice waterline (LIWL). These tests were carried out in the ice tank made free from ice. The bollard pull tests were repeated in the ice-free tank section (trim tank) immediately before the model was accelerated for the brash ice test. On the LIWL, a ventilating propeller was observed at high turning rates during bollard pull. This is not unusual for models on the LIWL. At 5 knots, this did not occur. To account for the air, this point was not considered in curve fitting. Tests in the brash ice channels were performed as towed propulsion tests with propeller load variation. For each test condition (ice thickness and draft), the model was towed through the entire brash ice channel without stopping. When conducting numerical validation, the speed control of the carriage was set to 0.474 m/s, which corresponds to 5 kn in full scale. The brash ice thicknesses for different ice classes are provided in Table 3.

Table 3. Thickness of brash ice under different ice classes.

Test No	Type of Test	Loading Condition	Target Brash Ice Thickness	Actual Brash Ice Thickness	Channel Width
11030	Brash Ice Channel	UIWL	1.452 (1A)	1.476	64.52 (2B)
12030	Brash Ice Channel	UIWL	1.251 (1B)	1.325	64.52 (2B)
01000	Bollard Pull Overload	UIWL	-	-	-
21030	Brash Ice Channel	LIWL	1.452 (1A)	1.586	64.52 (2B)
22030	Brash Ice Channel	LIWL	1.251 (1B)	1.250	64.52 (2B)
02000	Bollard Pull Overload	LIWL	-	-	-

The tests were analyzed according to HSVA's standard method for towed propulsion tests in ice. If the brash ice thickness of a partial test run deviated from the target brash ice thickness of the total test run, a thickness correction factor, $F_1(H_{avg})$, was applied to the resistance (to the measured pull force and thrust):

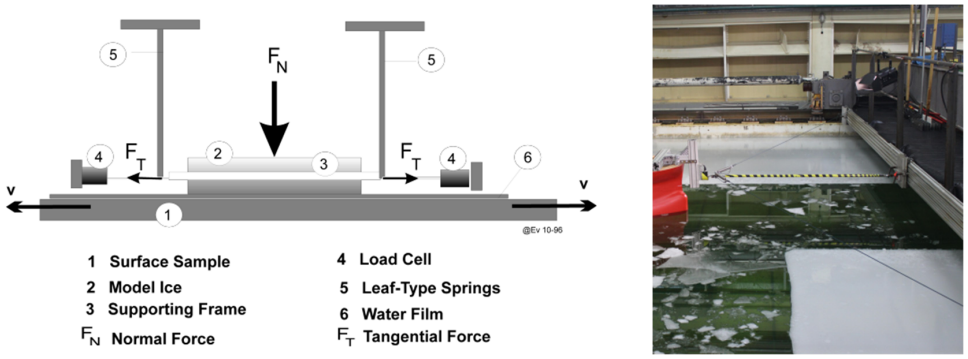
$$F_1(H_{avg}) = \left(H_{avg}^{target} / H_{avg}^{actual}\right)^{1.5-0.4F_{nHI}} \quad (8)$$

$$F_{nHI} = V / \sqrt{g \cdot H_{avg}} \quad (9)$$

where F_{nHI} is the froude number based on the ice thickness, V is the ship's speed, and H_{avg} is the average of brash ice thickness.

3.4. Test Performance

In order to obtain the required friction coefficient between the hull and ice, a wooden plate, which had been simultaneously painted with the model, was used for the friction test. For this purpose, a testing apparatus was used, the principal arrangement of which is shown in Figure 5a. Instead of the model, a wooden plate, which had been painted together with the model, was used for the friction test. The test plate was moved under the ice piece, which had been put upside down onto the test plate. The ice piece was held in place by a frame suspended from a bridge frame. The tangential force was measured with two slightly prestressed load cells mounted between the frame and the bridge frame. The normal load on the contact surface was applied by the weight of the ice piece plus a variable ballast weight. The friction tests were performed at a speed of 0.10 m/s. The friction coefficient was calculated according to Coulomb's friction law. After experimental testing, it was found that the ship–ice friction resistance coefficient range is 0.07–0.16. The friction coefficient between ship and brash ice in this article is 0.1, which meets the FSICR requirements.



(**a**) (**b**)

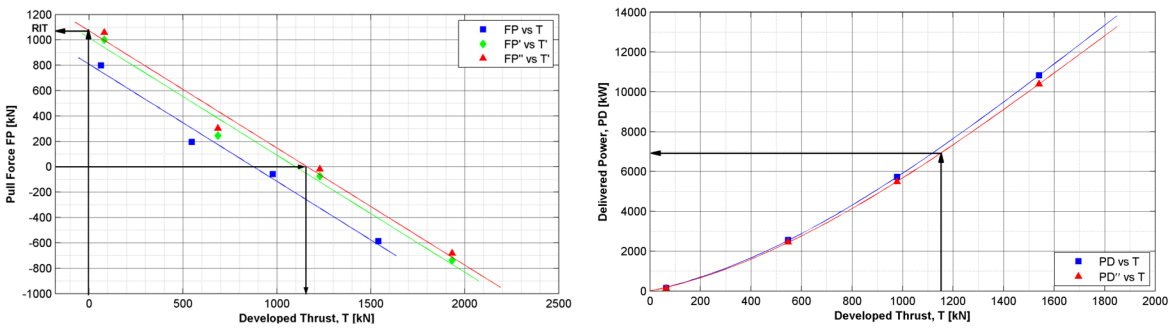
Figure 5. The towed propulsion tests. (**a**) Test device for measuring sea ice friction coefficient; (**b**) towed propulsion tests.

3.5. Towered Propulsion Results

When performing the towed propulsion test, the model is hauled by a carriage operating at a constant velocity, replicating conditions similar to those in a resistance test, while concurrently being actuated by its propulsor. The towing force is transmitted through a double-hinged pull rod and quantitatively assessed using a load cell positioned at the bow of the model. Throughout the testing procedure, the revolution rate is incrementally adjusted, typically undergoing four distinct stages. At the lowest revolution rate, the propulsor operates in proximity to the zero-thrust condition. Conversely, the highest revolution rate is chosen to ensure that the propulsor thrust exceeds the self-propulsion point, signifying that the model actively propels the carriage. During the test, the model remains unconstrained in terms of pitch and roll movements, while swaying and yawing within a pre-defined range are permissible. The pull rod primarily serves to maintain course stability. To mitigate the risk of excessive course deviations or the potential breakdown of the model, two transverse strings are affixed to the bow and pre-tensioned by springs, as illustrated in Figure 5b.

3.5.1. Total Resistance and Thrust in Brash Ice

Provided that the revolution rate is varied within a sufficiently wide range, the towed propulsion test is a suitable alternative to the pure towing test for determining the total resistance in ice. In this case, it is most appropriate to use the lowest revolution rate so that the propulsor thrust remains positive. Assuming that, for a constant speed, the thrust deduction fraction, t, is independent of the revolution rate or the propulsor load, linear regression is applied to the data of towing force, FP, vs. the developed propulsor thrust, T, as shown in Figure 6a. By using this regression function, the towing force for vanishing thrust is determined. The value obtained is in equilibrium with the total resistance in ice, RIT.



(**a**) (**b**)

Figure 6. The data of towed propulsion test (HSVA). (**a**) FP vs. developed propulsor thrust, T; (**b**) PD vs. developed propulsor thrust, T.

3.5.2. Developed Thrust and Delivered Power

The linear regression previously discussed serves as a tool to determine the developed thrust at the self-propulsion point. In this context, it is essential that the towing force, FP, attains a value equivalent to zero. At this time, we can determine the developed thrust. The self-propulsion power is determined through a regression analysis, which is applied to the measured data comparing the delivered power with the developed thrust. The delivered power, denoted as PD, during self-propulsion is ascertained by substituting the developed thrust into the regression function. Figure 6b shows the relationship between the delivered power and the developed thrust (T).

3.5.3. Propulsive Efficiency

Thrust coefficient K_T, torque coefficient $10K_{Q,}$ and efficiency η_0 for each advance coefficient are obtained from the calculated thrust and torque. The propulsive coefficients mentioned above are defined as follows:

$$J_V = V_A/nD \tag{10}$$

$$K_T = T/\rho n^2 D^4 \tag{11}$$

$$K_Q = Q/\rho n^2 D^4 \tag{12}$$

$$ETABV = T{\cdot}V/PD \tag{13}$$

$$ETABV0 = K_T/J_V \tag{14}$$

$$ETABV/ETABV0 = relative\ propulsor\ efficiency \tag{15}$$

where T and Q are the propeller thrust and torque, D is the diameter of the propeller, n is the rate of revolution, J_V is the advancing speed, and PD is the delivered power.

By comparing the propulsive efficiencies in ice and in ice-free water, ETABV and ETABV 0, respectively, the intensity of the propulsor–ice interaction can be quantified in terms of propulsive efficiency loss due to the presence of ice. For this purpose, relative propulsive efficiency based on thrust identity is calculated; i.e., the propulsive efficiency in ice is divided by the propulsive efficiency in ice-free water. The latter is determined from overload tests performed at the same model speed.

3.5.4. Thrust Deduction and Propulsive Efficiency in Ice

The accurate determination of thrust deduction in ice requires similar ice properties in resistance and propulsion tests. However, it has been observed that the thrust deduction fraction can be achieved with equal precision from towed propulsion tests. Assuming that the towing force equals resistance when the thrust is zero and that the relationship between the thrust and towing force is linear at a constant speed and variable revolution, the thrust deduction can be calculated from the linear regression slope, $t(V) = 1 - FP(V, T = 0)/T(V, FP = 0) = 1 + B_1(V)$.

The propulsive efficiency, ETAD, is determined through the comprehensive evaluation of the total ice resistance encountered and the actual delivered power.

$$ETAD = RIT{\cdot}V/PD \tag{16}$$

3.5.5. Corrections for Scale Effects

Comparisons of model tests and full-scale trials of different icebreaking hull forms have shown that the model icebreaking resistance scaled up according to Froude's scaling law correlates well with the full-scale resistance only for certain model ice thicknesses.

A good correlation is found for medium-model ice thicknesses. Slightly too optimistic predictions are obtained for thin-model ice. In the case of relatively thick-model ice, the scaled-up model resistance is significantly higher than the full-scale ship resistance. This fact is taken into account by applying a correlation correction. This correlation correction increases or decreases the model resistance depending on the model ice thickness.

$$RIT''_{Ship}(V) = \lambda^3\left[RIT'_{Model}(V) + i{\cdot}RIT'_{Model}(F_n = 0.05)\right] \tag{17}$$

$$i = 0.35(1 - HI/HI_0) \tag{18}$$

where HI is model ice thickness (target value), HI_0 is 45 mm, λ is the scaling factor, and RIT' (F_n = 0.05) is extrapolated/interpolated resistance at F_n = 0.05.

In principle, when analyzing towed propulsion tests, the (additive) correlation correction can be applied to one of the two forces, FP or T, which drive the model forward. The easier way is to add the correlation correction to the towing force FP.

$$FP''_{Ship}(V) = \lambda^3{\cdot}\left[FP'_{Model}(V) + i{\cdot}RIT'_{Model}(V = 0)\right] \tag{19}$$

Due to the lower Reynolds' number, the efficiency of the propulsor is lower in the model test than at full scale. Thus, when scaling up the power, an allowance of 4% was applied to the model test results. Moreover, the test results that were corrected using the model/full-scale correlation are marked with a double apostrophe.

$$PD''_{Ship} = 0.96\lambda^{3.5}{\cdot}PD_{Model} \tag{20}$$

4. Full-Scale Simulation Model

4.1. Propeller Open-Water Performance

Prior to the self-propulsion numerical simulation, the open-water performance of a propeller was examined, and the scaling ratio of the propeller was 1:29.508, adopting a realizable k-epsilon turbulence model. The center of the propeller hub was selected as the origin of the computational domain, and rotating and static domains were established separately. The base size of the grid was set to 0.2 m, the thickness of the first prismatic layer mesh was set to 0.004 m, the growth rate of the boundary layer grid was set to 1.2, and the number of layers was set to 6. The rotating domain was meshed with a polyhedral grid, and the grid around the propeller is shown in Figure 7a. The total grid number in the computational domain mesh was 1.71 million, with 1.12 million for the rotation region mesh and 0.59 million for the static region mesh. The propeller speed was fixed at 1.488 r/s in all simulations, and the range of the advance coefficient was increased from J = 0.05 to J = 0.7. The K_T, $10K_Q$, and η obtained through numerical simulations were compared with the experimental values. In addition, the propeller hydrodynamic performance under three sets of meshes (coarse, medium, and fine) was investigated. Figure 7b shows the hydrodynamic calculation results under the three sets of mesh; the number of coarse, medium, and fine mesh was 0.71 million, 1.37 million, and 2.79 million, respectively. It was found that the calculation results under the different grids were similar. In order to save computing resources, the medium mesh was selected for numerical calculations in the subsequent research.

Figure 7c shows a comparison between numerical calculations and experimental values for the open-water propeller. The numerical simulations were found to have good consistency with experimental results. Although the difference in η increased gradually with the increase in the advance coefficients, the error between simulation and experimental

values remained within 8%. Thus, the numerical method is capable of accurately predicting the open-water performance of the propeller.

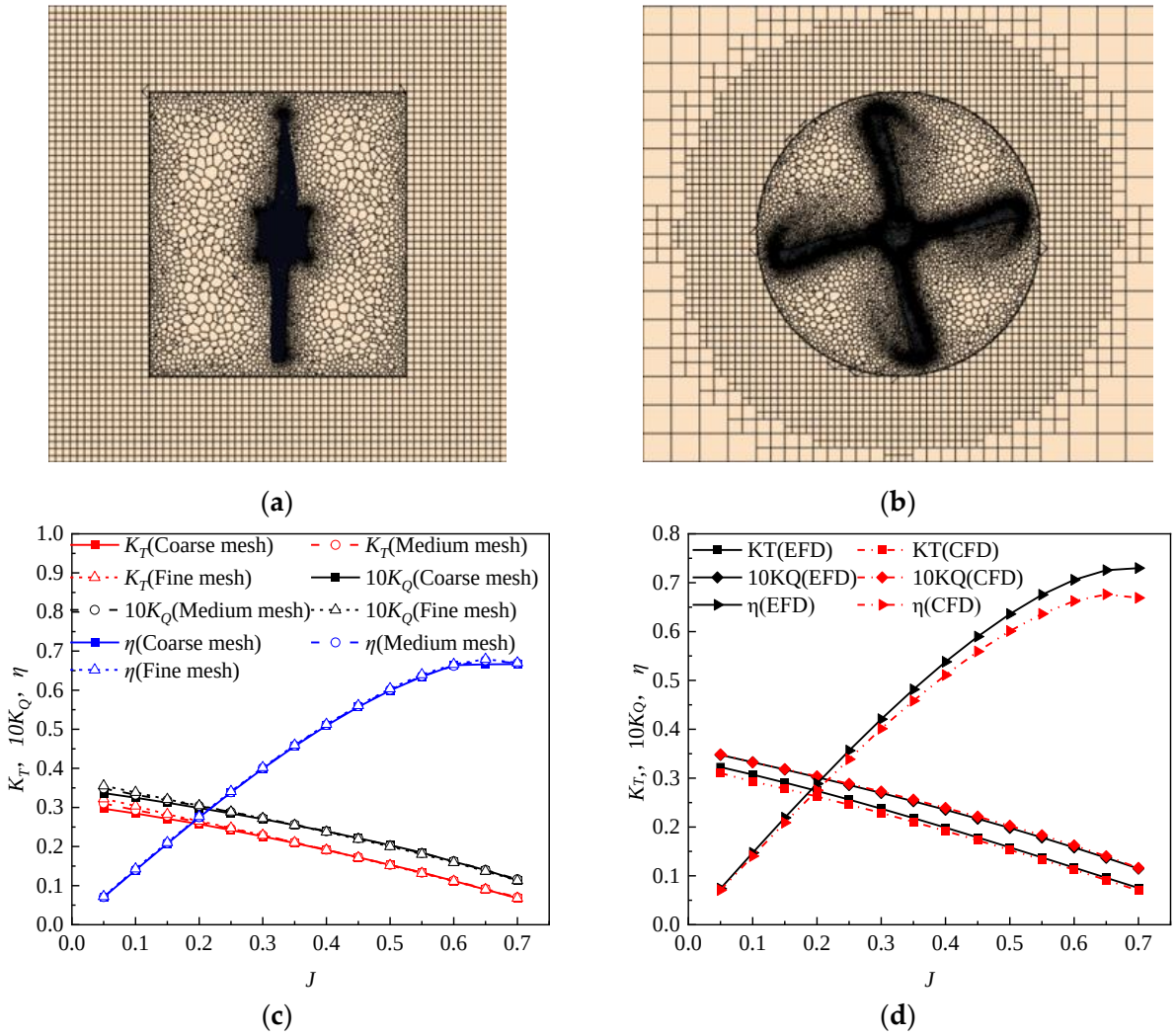


Figure 7. Numerical results of hydrodynamic performance of propeller. (**a**,**b**) Grid around the propeller. (**c**) Grid convergence verification. (**d**) Hydrodynamic calculation results.

4.2. Geometric Model and Computational Ice Tank

This study used the hull lines of a polar transport ship to construct a computational model of the full-scale ship. The ship underwent model testing in an HSVA ice tank. The ship's hull lines and the full-scale ship model are shown in Figure 8. The ship–ice collision process was simulated using the CFD-DEM approach, implemented in STAR-CCM+ software. Following the test conditions and relevant standards of the International Towing Tank Conference (ITTC), numerical grid partitioning was applied to the computational ice tank.



Figure 8. The computational model of the 68k MPV vessel.

During the numerical simulation of ship–ice collision, the computational domain was created around the ship to solve the flow field both in the model and in ice particles. The X-axis direction is the hull speed direction, the Y-axis direction is the hull width direction, and the Z-axis direction is the pool height direction. In order to ensure sufficient contact between the ship and the broken ice, the calculation domain of the brash ice channel was established based on the HSVA ice tank test standard. The range of the x-axis direction is $-2.0\text{Lpp} \leq x \leq 3.0\text{Lpp}$. The range of spanwise direction is $-2.0\text{Lpp} \leq x \leq 2.0\text{Lpp}$, and the range of vertical direction is $-2.0\text{Lpp} \leq z \leq 1.0\text{Lpp}$. The width of the brash ice channel is twice that of the ship's breadth. The full-scale computational model of the polar transport ship corresponds to Figure 9. The dimensions of the computational domain and the distance between the ship and the level ice region are shown. In the numerical simulation, a relative motion approach was employed, where the ship was treated as a rigid body. The ice particles were introduced into the water surface through a grid representation method. This method determined the position, direction, and concentration of the ice particles being injected.

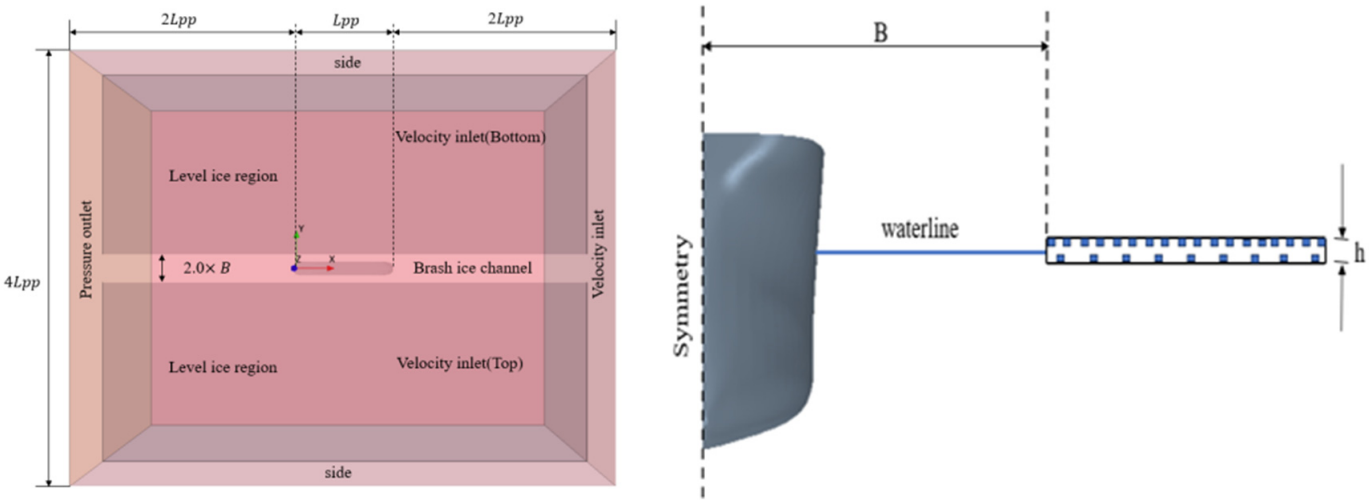


Figure 9. The computational domain of the 68k MPV vessel in brash ice channels.

4.3. Mesh Partition and Boundary Conditions

When performing numerical calculations, both calculation accuracy and computing resources must be taken into consideration. Therefore, corresponding grid densification processing was carried out based on physical phenomena in local areas such as the hull waterline, injector position, water surface, and Kelvin wave area. The mesh around the hull and the computational domain was generated using trimmed and prismatic layer mesh generators, while the propeller and its rotating domain were meshed using a polyhedral mesh generator. This section illustrates the mesh distribution around the hull and propeller with a medium grid size. The refined mesh is shown in Figure 10.

The conditions for the boundaries are provided in Table 4. The right boundary of the computational domain was set as the velocity inlet; the left boundary was designated as the pressure outlet; and the upper, bottom, and side boundaries were set consistent with the inlet boundary conditions. The hull surface and the level ice region were set as non-slip wall boundary conditions, while the injection of ice particles was performed using a component injector.

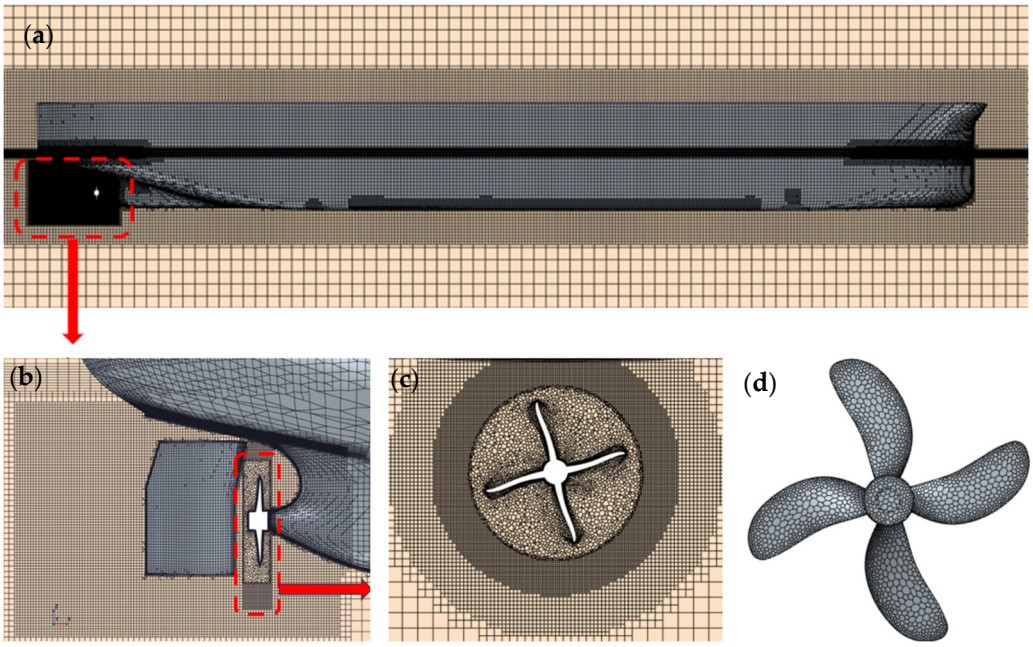


Figure 10. Distribution of the hull and surrounding mesh (medium mesh). (**a**) The grid around the hull (**b**) The grid near the propeller-rudder (**c**) The rotation domain grid (**d**) The propeller grid.

Table 4. Boundary of the computational domain.

Boundary	Boundary Condition
Water Inlet	Velocity inlet; the velocity is equal to the towing speed of ship model
Water Outlet	Pressure outlet; the outlet pressure is the hydrodynamic pressure
Bottom/Side/Top	Consistent with velocity inlet
Ship Wall	A non-slip wall boundary condition
Level ice region	Non-slip wall
Free surface	VOF free surface
Particle inject	Surface injection conditions for particles based on particle injection

5. Parametric Study Results

5.1. Analysis of Ship Collision Phenomena and Numerical Methods

A self-propulsion model test of a polar transport ship was conducted by HSVA. To realistically simulate the self-propulsion of ships in a brash ice channel, a model ice tank was established, and the results of the experiment conducted by HSVA were compared with the numerical simulation results. Figure 11 illustrates the interactions among the ship, propeller, rudder, ice, and flow, revealing that the polar transport ship, while navigating through the brash ice area, experiences noticeable flipping and stacking of ice particles at the bow after a certain duration. Under brash ice conditions, the primary sources of ice resistance stem from collisions, squeezing, and accumulation between the ship and ice. Broken ice at the bow is continuously pushed aside due to the ship's impact. Some of the broken ice slides along the sides of the ship under the influence of the flow, creating an ice-free area at the stern approximately equal to the width of the ship. Due to the close distance between the propeller and the broken ice in the design draft conditions of the polar transport ship, the broken ice around the propeller is sucked by the propeller. Under the joint action of the ship, propeller, rudder, and fluid, the broken ice particles near the propeller show an obvious up-and-down oscillating motion. This observation aligns with relevant model experiments. Our team has verified the same numerical method for the AFRAMAX oil tanker towing model tested in HSVA [15,29], indicating that the combined

CFD and DEM numerical simulation method can reasonably simulate the interaction between the ship, ice, propeller, rudder, and flow very well.

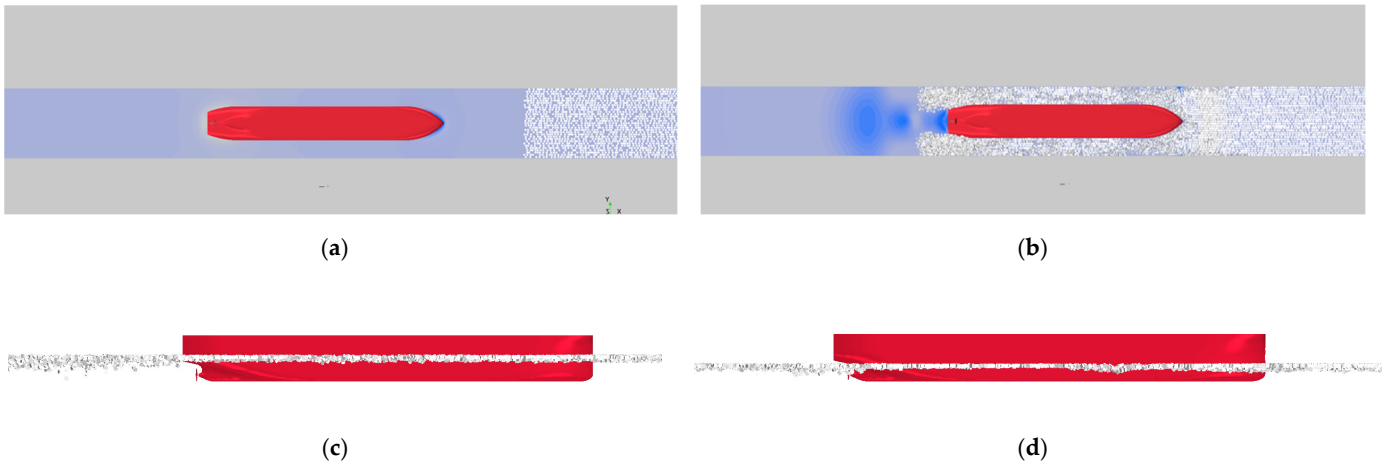


Figure 11. Flow field variation map of ship–ice–flow interaction. (**a**) The initial arrangement of the brash ice; (**b**) ship entered the brash ice area completely; (**c**) scantling draft condition; (**d**) design draft condition.

5.2. Mesh Independence Verfication

To validate the reliability of the DEM method, model experiments were conducted on a polar transport ship model in an HSVA ice tank. The total resistance of the ship comprised the ice resistance and water resistance. The ice loads on the ship in the x, y, and z directions constituted the total ice loads on ships. The numerically calculated ice resistance and water resistance were compared and validated against experimental predictions and the FSICR formula. For a grid independence analysis, three grid densities were generated, coarse (2.51 million), medium (3.29 million), and fine (4.25 million), with a mean refinement ratio of 1.2 and a grid refinement factor of $r_G = \sqrt{2}$. In a convergence study conducted to validate the results, a representative case was selected in the brash ice area, with a ship speed of 5 kn. A grid convergence analysis was conducted by refining the grid sizes, and numerical errors and uncertainties induced by spatial and temporal discretization were assessed. As shown in Figure 12c, under open-water conditions, the water resistance under the medium grid was closest to the experimental predicted value. The water resistance calculated under the medium mesh was 88.88 kN, while the model-scale experiment predicted a water resistance of 94.1 kN for the full-scale ship, resulting in an error of less than 6%. Under the 1A ice class conditions, the total resistance calculated using the FSICR formulas was 1357.1 kN. Table 5 discusses the discrepancies between the ice resistance obtained from the numerical calculations under the different mesh quantities, the experimental predictions, and the FSICR formula. The inconsistency in the ice resistance calculation results under the different mesh densities was due to the fact that the finer mesh had a better ability to capture the localized stress concentration in the ship-ice contact region than the coarser mesh. Additionally, as the broken ice was assumed to be a rigid body, with no deformation considered, mesh refinement led to more detailed collision forces. Figure 12 shows the ice resistance and water resistance grid independence calculation results for the upper ice waterline (UIWL). Therefore, the CFD-DEM method adopted in this study was deemed reliable.

The convergence ratio R_G was 0.795, which indicates that the ice resistance obtained from the CFD simulation shows a monotonic convergence in this study. The total ice resistance and water resistance obtained from numerical calculations, considering both computational errors and computational efficiency, were found to be the closest to those

obtained from the experimental tests. The medium grid number (3.29 million) was selected in this study.

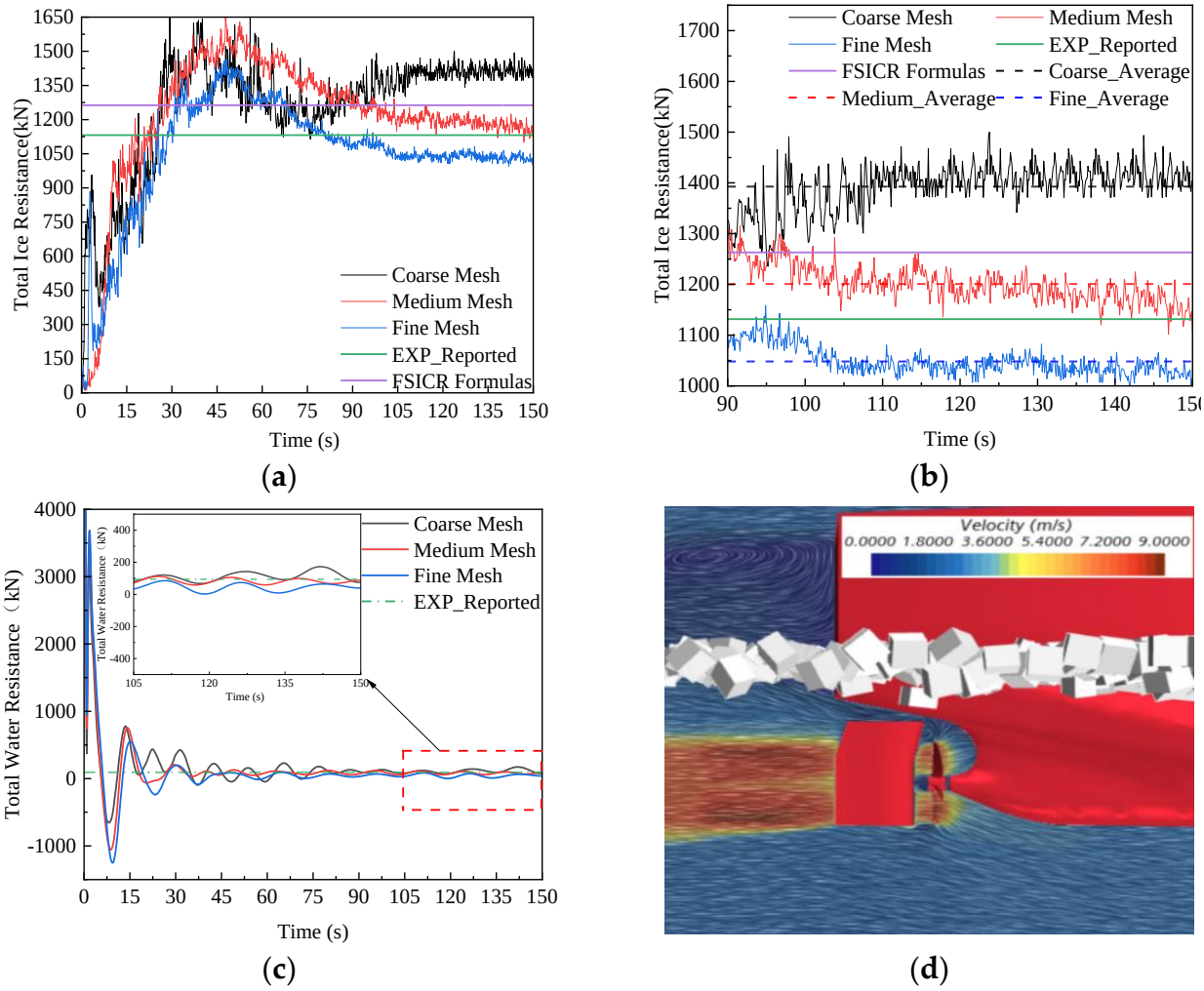


Figure 12. Numerical computation result: (**a**) total ice resistance verification of 3 grids; (**b**) 90 s–150 s ice resistance time history curve after stabilization; (**c**) water resistance under 3 grids; (**d**) flow field.

Table 5. Full-scale ice resistance predictions based on experiments and FSICR result under UIWL condition.

Condition	Grid Density	Grids Number	CFD (KN)	EXP_ Results	FSICR Formulas	Error (%)	r_g	R_G	P_G	C_G	U_G (%)
UIWL 1A	Coarse	2.51 M	1392.515	1131.6	1263.0	23.06	1.192	0.795	1.306	0.613	5.913
	Medium	3.29 M	1200.764			6.11					
	Fine	4.25 M	1048.281			−7.36					

R_G, P_G, C_G, and U_G represent the convergence ratio, estimated order of accuracy, asymmetric range, and grid uncertainty, respectively. The specified definition formulas could reference the Verification and Validation guidelines of ITTC [30].

5.3. Self-Propulsion Analysis

5.3.1. Acquisition of Self-Propulsion Points of Scant Draft

In a towed ice tank self-propulsion test, it is necessary to choose a reasonable propeller rotation speed. Because of the large fluctuation of the ice resistance on the ship, for the determination of the self-propulsion point, multiple propeller speeds often need to be set. In our study, the full-scale self-propulsion point was predicted using the equal rotational speed of the propeller variable similar to the model test. As friction resistance correction

was not considered in the full-scale calculation, the propeller velocity at the self-propulsion point could be determined when the propeller-produced thrust was balanced with the full-scale resistance. To clearly observe the numerical results of the polar transport ship moving through the brash ice channel in self-propulsion mode, in this section, the scantling and design draft conditions were taken into account. Multiple propeller speeds were selected, and Figure 13 shows the total resistance, thrust, and torque under different brash ice thickness conditions at the scantling draft.

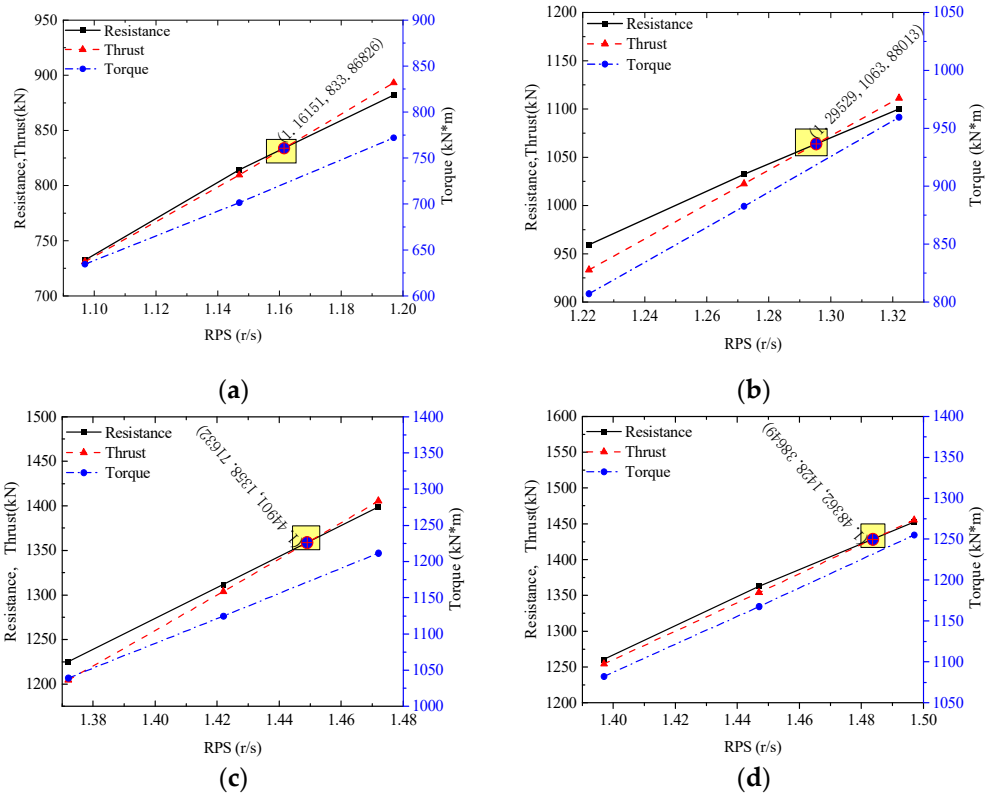


Figure 13. Results of self-propulsion test (UIWL). (**a**) Brash ice thickness 1.251 m, UIWL, (**b**) brash ice thickness 1.325 m, UIWL, (**c**) brash ice thickness 1.452 m, UIWL, (**d**) brash ice thickness 1.476 m, UIWL.

By changing the propeller speed at equal intervals, after the self-propulsion point was obtained, the corresponding rotational speed, thrust, and torque could be obtained via linear fitting interpolation according to the self-propulsion test curve of the ship model. After interpolation calculation, when the brash ice thicknesses were 1.251 m, 1.325 m, 1.452 m, and 1.476 m, the propeller speeds when the total resistance and thrust were balanced were 1.162 r/s, 1.295 r/s, 1.449 r/s, and 1.484 r/s, respectively. Then, the resistance of the ship, the effective power of the ship, the power received by the propeller, and the propulsive efficiency were obtained. Through testing and numerical simulations, it was found that, at the same brash ice concentration, as the brash ice thickness increased, the ships needed a greater icebreaking capacity to keep moving. In this case, it was necessary to increase the propeller speed in order to improve the ship's power; it was also necessary to consider whether the propeller and hull strength could withstand the resulting extra load. Figure 14 shows the distribution of the velocity field behind the ship–propeller–rudder under the scan draft of a full-scale ship, with target brash ice thicknesses of 1.251 m (1B) and 1.452 m (1A).

As shown in the figure, under the joint action of the propeller rotation and rudder, a long acceleration area appears in the rear flow field of the rudder. With the increase in the propeller speed, the flow velocity near the blade gradually increases, but the flow velocity behind the hub decreases. The water flows uniformly over the surface of the propeller,

making the pressure on the blade surface greater than that on the back of the blade, and the thrust is generated by this pressure difference.

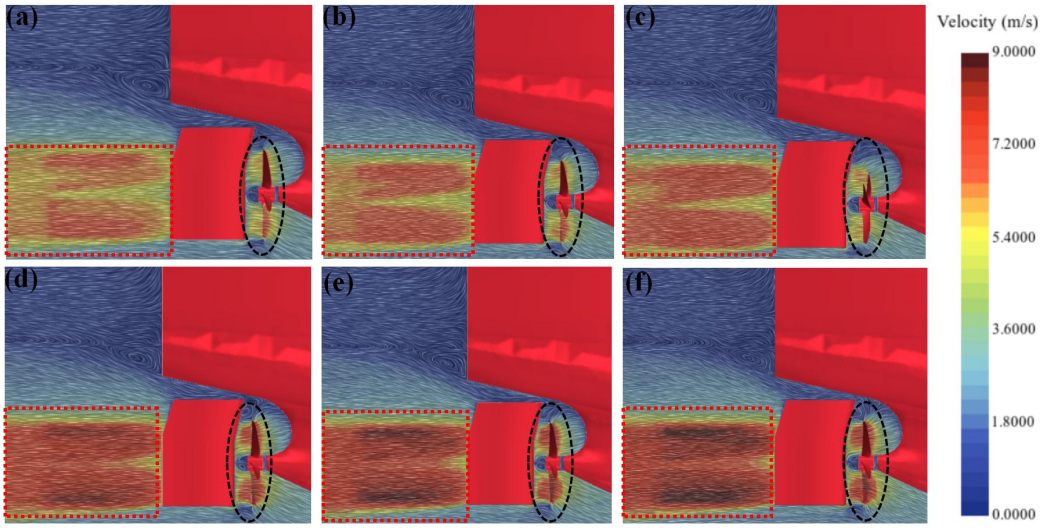


Figure 14. Velocity field (**a**) brash ice thickness 1.251 m—1.097 r/s; (**b**) brash ice thickness 1.251 m—1.147 r/s; (**c**) brash ice thickness 1.251 m—1.197 r/s; (**d**) brash ice thickness 1.452 m—1.372 r/s; (**e**) brash ice thickness 1.452 m—1.422 r/s; (**f**) brash ice thickness 1.452 m—1.472 r/s.

5.3.2. Acquisition of Self-Propulsion Points of Design Draft

Figure 15 shows the changes in the total resistance, thrust, and torque under the design draft conditions when the brash ice thickness is 1.250 m, 1.251 m, 1.452 m, and 1.586 m.

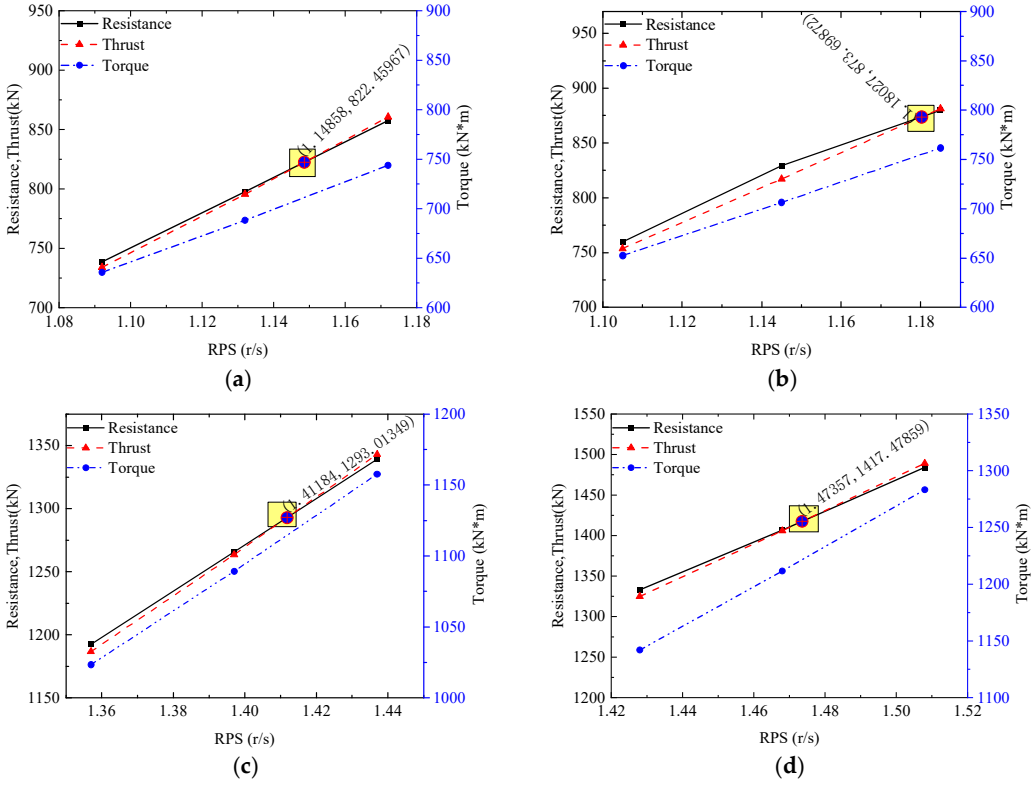


Figure 15. Results of full-scale self-propulsion test (LIWL). (**a**) Brash ice thickness 1.250 m, LIWL, (**b**) brash ice thickness 1.251 m, LIWL, (**c**) brash ice thickness 1.452 m, LIWL, (**d**) brash ice thickness 1.586 m, LIWL.

After interpolation calculation, it was found that when the brash ice thickness is 1.250 m, 1.251 m, 1.452 m, and 1.586 m, the total resistance and thrust are balanced, and

the propeller speeds are 1.149 r/s, 1.180 r/s, 1.412 r/s, and 1.474 r/s, respectively. At the same brash ice concentration and brash ice thickness, the propeller speed required to reach the self-propulsion point in the design draft is smaller than that required in the scant draft. There is a close relationship between the propeller rotation speed and draft depth. The propeller needs different propulsion powers under different draft conditions. A shallower draft makes the ship less stable, and the total resistance response decreases due to the lower wet surface area. Therefore, under the design draft conditions, the ship only needs a low propeller rotation speed to generate a certain thrust to overcome the total resistance. The total resistance, thrust, and torque at the self-propulsion point under the design draft conditions are obtained using numerical calculations. Figure 16 shows the surface pressure of the propeller–rudder system and the streamline distribution at different propeller rotation speeds under the design draft conditions.

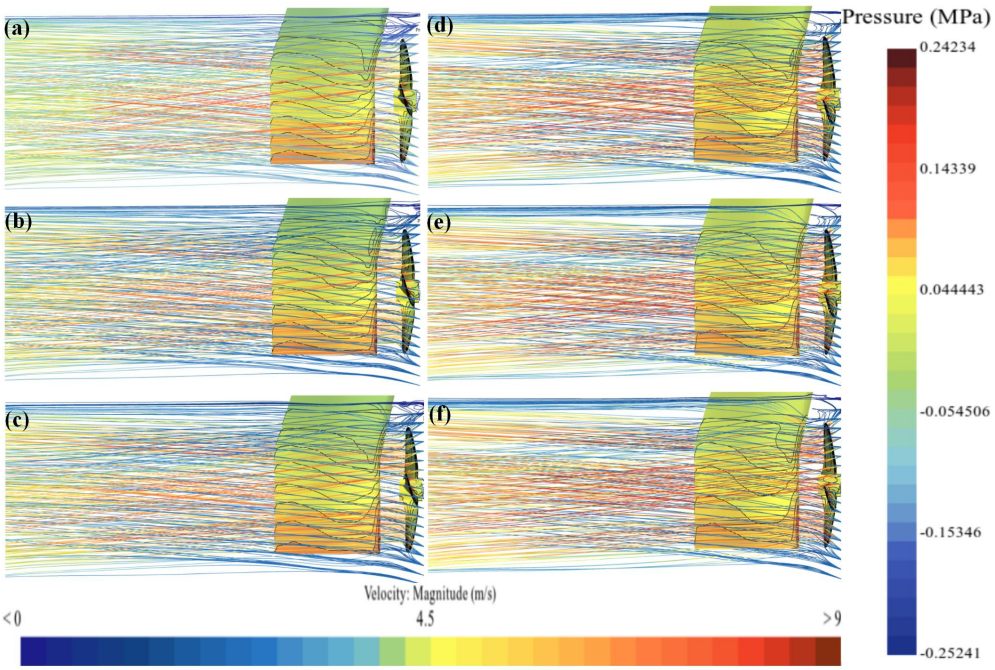


Figure 16. Velocity field surface pressure and streamline distribution of propeller–rudder system: (**a**) brash ice thickness 1.251 m—1.105 r/s; (**b**) brash ice thickness 1.251 m—1.145 r/s; (**c**) brash ice thickness 1.251 m—1.185 r/s; (**d**) brash ice thickness 1.452 m—1.357 r/s; (**e**) brash ice thickness 1.452 m—1.397 r/s; (**f**) brash ice thickness 1.452 m—1.437 r/s.

When the fluid flows through the rudder surface, a low-pressure area and a high-pressure area form along the upper and lower surfaces of the rudder's longitudinal profile, and the upstream face of the rudder forms a high-pressure area. The presence of the rudder has a rectification effect on the propeller's wake and improves the tail flow field of the propeller. When the propeller rotation speed increases, the wake of the propeller does not change dramatically. However, the pressure variation range of the rudder and propeller surface shows an increasing trend.

5.4. Presentation and Discussion of the Test Results

5.4.1. Comparison of Numerical Simulation and Experiment for UIWL

To understand the influence of the brash ice thickness, self-propulsion model tests under four brash ice thicknesses were carried out under scant draft conditions. The full-scale performance prediction for the investigated brash ice conditions is summarized. The ship's speed is 5 kn. In the self-propulsion of the polar transport ship in the brash ice area, multiple sets of propeller rotation speeds are selected for numerical simulations of each

group of brash ice thickness. When the propeller rotation speeds are 1.222 r/s, 1.447 r/s, 1.197 r/s, and 1.422 r/s, the errors between the total resistance, total thrust, delivered power, and propulsive efficiency and the experimental values are the smallest. Table 6 (UIWL) provides a comparison between the experimental data and numerical simulation results. These results indicate that the brash ice thickness has a significant impact on total resistance, with the numerical calculated total resistance error being within 10.51%. The propeller speed has a significant impact on the required total thrust, with the errors in the total thrust at different propeller rotation speeds being within 2.41%. The propeller rotation speed and torque together determine the delivered power. The difference between the delivered power and propulsive efficiency is under 34.32% and 15%, respectively. As the broken ice thickness increases, the ship experiences greater ice resistance. At the same time, the propeller rotation speed of the ship needs to increase in order to generate more thrust to overcome the ice resistance. As a result, the delivered power gradually increases, consuming more energy and leading to a decrease in propulsive efficiency. By substituting the ice load calculated in the simulation into the calculation formula of the Finnish-Swedish Ice Class Rules, it is observed that the main engine power calculated using the empirical formula is excessively high, with the maximum error reaching 83.28%. Therefore, compared to the experimental results, the numerical simulation method produces relatively reasonable results.

Table 6. The results of propulsion tests (UIWL).

UIWL	Brash Ice Thickness of Model Test (m)	Total Resistance Ri (kN)	Required Total Thrust T (kN)	Delivered Power Pd (kW)	Propulsive Efficiency ηd
EXP_Reported	1.325 (Actual)	928.10	956.30	5333.20	0.448
CFD_simulation		959.31	933.30	6194.04	0.398
Error (%)		3.36%	−2.41%	16.14%	−11.16%
EXP_Reported	1.476 (Actual)	1233.00	1361.10	8643.40	0.367
CFD_simulation		1362.54	1353.78	10,610.08	0.330
Error (%)		10.51%	−0.54%	34.32%	−10.08%
EXP_Reported	1.251 (1B, Target)	860.10	885.80	4813.30	0.460
CFD_simulation		881.97	890.96	5803.02	0.391
Error (%)		2.54%	0.58%	20.56%	−15.00%
EXP_Reported	1.452 (1A, Target)	1206.50	1331.80	8386.80	0.370
CFD_simulation		1311.50	1303.79	10,043.48	0.336
Error (%)		8.70%	−2.10%	19.75%	−9.19%

Due to the structural draft conditions, the maximum broken ice thickness is 1.476 m, requiring a higher propeller rotation speed to balance the total resistance and thrust. As a result, the ship experiences the highest total ice resistance and propeller torque. Therefore, the delivered power obtained from the numerical calculation is the highest, and the error between the numerical results and the experimental values is the largest. According to the Finnish-Swedish Ice Class Rules, the ship is required to ensure continuous navigation in brash ice channels at a speed of 5 kn, and the main engine power is determined accordingly. Here, the actual and target ice thicknesses are selected, and the maximum speed is 5 kn. According to the calculation, Figure 17 shows the changing trend of the total resistance, total thrust, delivered power, and effective power, and the data are fitted.

In this section, numerical and experimental methods are used to study the effect of brash ice thickness on ice load and the effect of propeller speed on total thrust. Figure 17 shows that the overall change trend of the ice load under four brash ice thicknesses is relatively consistent. With the increase in the brash ice thickness and propeller speed, the total resistance, total thrust, and delivered power of the ship under self-propulsion conditions in brash ice areas all increase, and the results show an exponential trend. This is because with the increase in the brash ice thickness, the contact area between the ship and ice increases, resulting in an increase in the contact force between the ship and the ice. At

the same time, it is necessary to make the ship sail at a speed of 5 kn, and the total thrust must be greater than the total resistance of the ship. Therefore, the total thrust increases with the increase in the brash ice thickness. In the model test, the delivered power of the full-scale ship under the scantling draft conditions changes with the brash ice thickness, and the variation law of the engine output power with the brash ice thickness is obtained by fitting. It is found that the results of the bollard tests showing the full-scale model test prediction data in the brash ice area and the ice-free area have a good correlation. By fitting the numerical results of the effective power with the experimental results, it is found that the error between the numerical results and the experimental results is less than 10.51%.

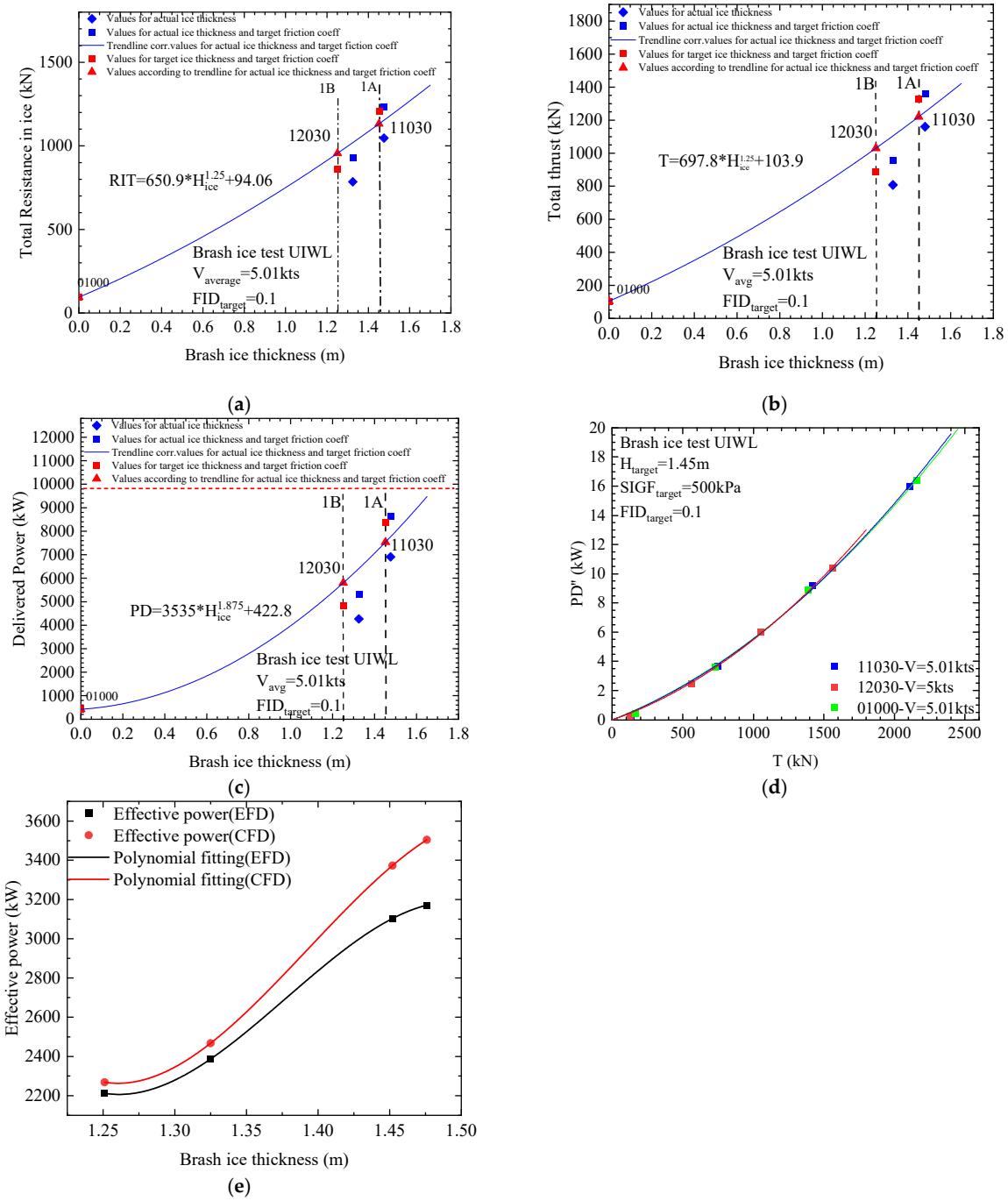


Figure 17. The full-scale performance prediction for brash ice condition UIWL. (**a**) Total resistance; V = 5 kn; (**b**) required propeller thrust vs. brash ice thickness; (**c**) required power vs. brash ice thickness; (**d**) propeller performance in broken ice and in ice-free water; delivered power vs. developed thrust; (**e**) effective power vs brash ice thickness.

5.4.2. Comparison of Numerical Simulation and Experiment for LIWL

To obtain the hydrodynamic performance of the full-scale ship under lower ice waterline (LIWL) conditions with various ice class rules, numerical simulations are conducted for the actual brash ice thicknesses and target brash ice thicknesses. The rotation speeds of the four groups of full-scale propellers under the brash ice thickness conditions are 1.092 r/s, 1.468 r/s, 1.105 r/s, and 1.357 r/s. Table 7 provides the total resistance, total thrust, delivered power, and propulsive efficiency of the ship under different operating conditions, along with errors compared to the experimental values.

Table 7. The results of propulsion tests (LIWL).

LIWL	Brash Ice Thickness of Model Test (m)	Total Resistance Ri (kN)	Required Total Thrust T (kN)	Delivered Power Pd (kW)	Propulsive Efficiency ηd
EXP_Reported	1.250 (Actual)	752.10	791.50	4104.80	0.472
CFD_simulation		738.60	795.47	4893.24	0.419
Error (%)		−1.79%	0.50%	19.21%	−11.23%
EXP_Reported	1.586 (Actual)	1297.80	1397.10	8860.00	0.377
CFD_simulation		1406.71	1405.89	11,170.16	0.324
Error (%)		8.39%	6.29%	26.07%	−14.06%
EXP_Reported	1.251 (1B, Target)	752.60	792.10	4109.10	0.472
CFD_simulation		759.62	753.63	4528.51	0.431
Error (%)		0.93%	−4.86%	10.21%	−8.69%
EXP_Reported	1.452 (1A, Target)	1157.90	1246.10	7558.10	0.394
CFD_simulation		1192.62	1186.66	8720.78	0.352
Error (%)		2.99%	−4.77%	15.38%	−10.66%

It can be clearly observed in Table 7 that, under LIWL conditions, the change in the brash ice thickness has a great influence on the total resistance. By comparing the above four cases, it can be observed that, by changing the brash ice thickness, the total resistance under the test value increases by 0.726 times, the total resistance under the numerical calculation increases by 0.905 times, and the error between the numerical calculation and the test value is within 8.39%. With the increase in the brash ice thickness and propeller speed, for the calculation result of the total thrust, the error between the numerical calculation value and the test value is within 6.29%, the delivered power error is within 26.07%, and the maximum error of propulsive efficiency reaches 14.06%.

Figure 18 illustrates the variations in the total resistance, total thrust, delivered power, and effective power of the polar ship under design draft conditions as a function of brash ice thickness. Unlike the structural draft conditions, where the water resistance is 94.1 kN, the water resistance under open-water conditions with zero ice thickness is 44.24 kN. Through model tests and numerical simulations, it is observed that, for a constant ice concentration and fixed ship speed of 5 knots, the contact area between the ship and broken ice under the design draft conditions is smaller than that under the structural draft conditions. Consequently, the ice load and water resistance experienced by the ship are reduced. Figure 18b shows that the total thrust increases with the brash ice thickness. As the ice thickness increases, the ice load increases, necessitating a higher propeller rotation speed to overcome the ship's total resistance. Thus, the total thrust increases with the increase in the brash ice thickness. In the design process of polar ships, the ship resistance calculation is crucial for estimating the main engine power and effective power under various ice conditions. The figure shows the functional relationship between the main engine power, the effective power, and the broken ice thickness when the broken ice concentration and ship speed are fixed. Through polynomial fitting, the function relation of the delivered power with the brash ice thickness is $PD = 3343 * H_{ice}^{1.875} + 181.2$. It is noted that the discrepancy between the numerical calculations and experimental results

for effective power under different ice thicknesses is similar to that observed under the scantling draft conditions. The effective power obtained by the numerical calculation is greater than the effective power of the test value. The effective power increases with the increase in the ice thickness, with the maximum discrepancy reaching 8.39%.

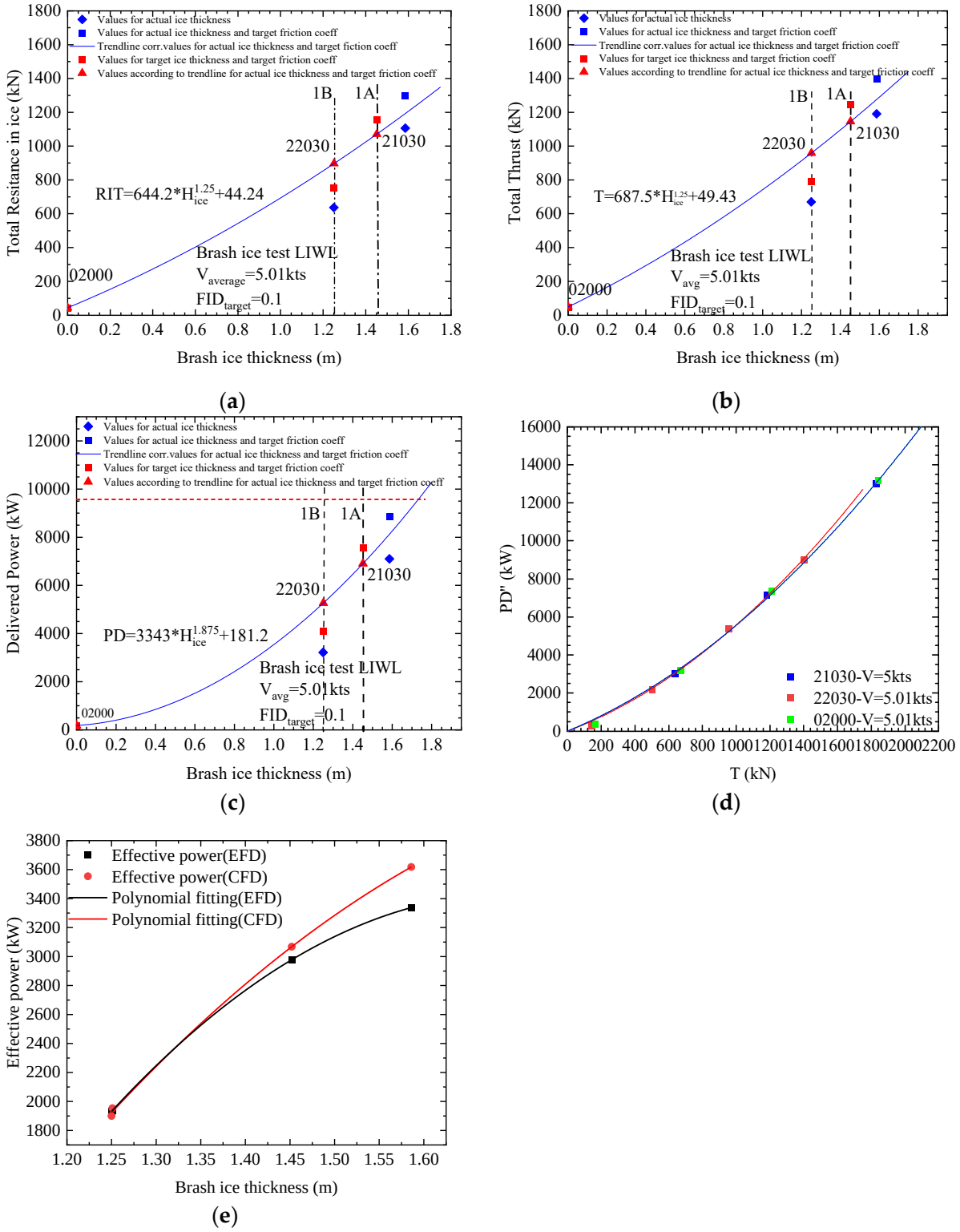


Figure 18. The full-scale performance prediction for brash ice condition LIWL; (**a**) total resistance; V = 5 kn; (**b**) required propeller thrust vs. brash ice thickness; (**c**) required power vs. brash ice thickness; (**d**) propeller performance and in ice-free water; delivered power vs. developed thrust; (**e**) effective power vs brash ice thickness.

5.4.3. Empirical Formulas for Brash Ice Resistance Estimation

The full-scale ship was tested for upper ice waterline (UIWL). Juva and Riska [31] did not consider the ship's speed and designed an empirical formula for the prediction of ice load on ships in brash ice. Spencer and Jones [32] used model tests to establish an empirical formula to predict the resistance of brash ice. The empirical formula proposed by DuBrovin has been proven to predict the brash ice resistance reasonably [33]. The ice resistance under different conditions of brash ice thickness was calculated according to three empirical formulas, the calculation results were compared with experiment data, and the error between the empirical formula calculation results and experiment data is shown in Table 8. For easy comparison, the corresponding results are drawn in Figure 19.

Table 8. Comparison of simulation, experimental, and empirical calculated ice resistance in brash ice condition (UIWL).

Ice Thickness/m	Simulation (kN)	Experimental (kN)	Empirical Calculated (kN)			Numerical Error (%)		
			Juva and Riska	Spencer	DuBrovin	Juva and Riska	Spencer	DuBrovin
1.251 (1B)	787.87	766.00	1083.87	855.72	899.56	41.49	11.71	17.44
1.325	865.21	834.00	1151.53	912.69	924.01	32.29	9.44	10.79
1.452 (1A)	1131.11	1112.40	1270.22	1011.48	985.81	14.24	−9.07	−11.38
1.476	1166.34	1138.90	1292.92	1030.46	995.52	13.52	−9.52	−12.24
Average Error (%)						25.38	0.64	1.15

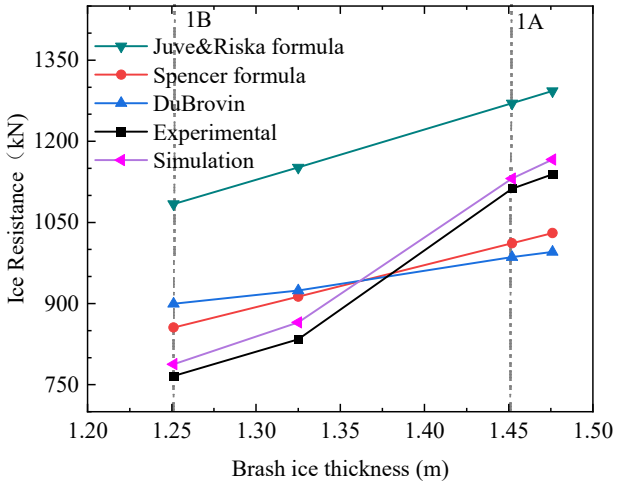


Figure 19. Experimental and empirical calculated ice resistance in brash ice condition (UIWL).

The numerical simulation results of the ice resistance agree well with the experimental results, followed by the Spencer empirical formula results, with the smallest average error of 0.64%. The gap between the Juva & Riska formula and experimental results decreases as the ice thickness increases, and the error between the Juva and Riska formula and experimental value is the largest. The ice resistance calculated using the Juva and Riska and DuBrovin empirical formulas is linearly related to the brash ice thickness. When calculations are performed using empirical formulas, potential biases in the ice load results may arise from variations in the ice concentration, ice shape, ship speed, and the ice physical parameters, and all of these can significantly impact the ice load on the ship.

The full-scale ship was tested on the lower ice waterline (LIWL). Comparisons of the empirical formula and experimental and numerical simulation results of the ice resistance are shown in Table 9. Comparisons between the numerical simulation, empirical formula, and model test results are shown in Figure 20.

Table 9. Comparison of simulation, experimental, and empirical calculations of ice resistance in brash ice condition (LIWL).

Ice Thickness/m	Simulation (kN)	Experimental (kN)	Empirical Calculated (kN)			Numerical Error (%)		
			Juva and Riska	Spencer	DuBrovin	Juva and Riska	Spencer	DuBrovin
1.250	694.40	707.90	1049.48	570.10	907.80	48.25	−19.47	28.23
1.251 (1B)	715.42	708.40	1051.34	570.18	908.25	48.41	−19.51	28.21
1.452 (1A)	1148.42	1148.70	1237.69	680.81	995.89	11.13	−38.87	−10.58
1.586	1288.82	1288.82	1364.70	756.14	1052.26	8.86	−39.68	−16.06
Average Error (%)						29.16	−29.38	7.45

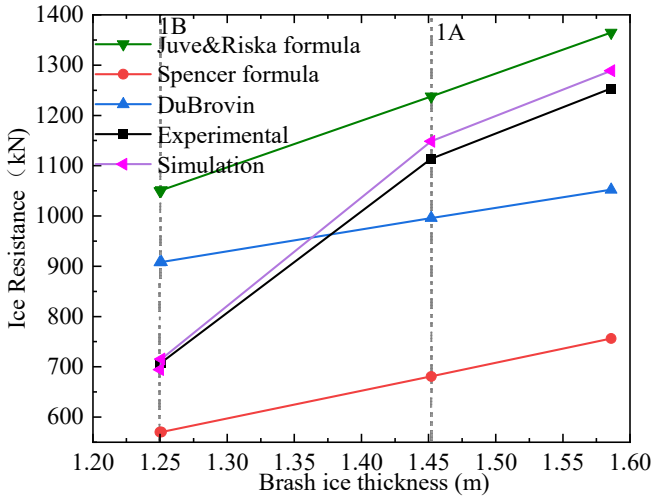


Figure 20. Experimentally and empirically calculated ice resistance in brash ice condition (LIWL).

The brash ice resistance under different working conditions was numerically simulated, and the errors between the Juva and Riska empirical formula, Spencer empirical formula, DuBrovin empirical formula, and model tests were compared. When using the Juva and Riska formula, the influence of speed was not considered, and the brash ice thickness had a greater influence on the ice resistance. Regarding the empirical formulas, the ice resistances obtained by the Juva and Riska, Spencer, and DuBrovin empirical formulas were linearly related to the brash ice thickness. The Spencer empirical formula results were smaller than the model test results. Among the three empirical formulas for calculating the brash ice resistance, the Spencer empirical formula resulted in the smallest ice resistance, and the error between its value and the test value was the largest, with the average error reaching 29.38%. The average error of the DuBrovin empirical formula was the smallest and closer to the model test results. In general, under lower ice waterline (LIWL) conditions, the numerical simulation is more stable and accurate than the empirical formula.

6. Conclusions

The DEM method was used to numerically simulate the self-propulsion performance of polar transport ships under brash ice channel conditions, which can effectively simulate the interaction process between the full-scale ship, propeller, rudder, and brash ice. The total ice resistance, total thrust, effective power, propulsive efficiency, and delivered power of the polar transport ship under different draught conditions were studied separately. It was found that the numerical results are in good agreement with experimental values and the empirical formula calculation results, and the following conclusions are drawn:

(1) The CFD-DEM method can reasonably simulate the self-propulsion of an ice class polar transport ship and capture the flow field near the ship, propeller, and rudder. Under design draft conditions, the brash ice is sucked by the propeller due to its rapid rotation.

(2) Numerical simulations were conducted on the open-water hydrodynamic performance of a polar transport ship's propeller, and K_T, $10K_Q$, and η were compared with experimental values. The maximum error in efficiency is within 8%, which is within a reasonable range of error.

(3) The self-propulsion points of the polar transport ship under the scantling and design draft conditions were obtained, and the corresponding propeller rotation speed, thrust, and torque were obtained after linear fitting and interpolation. Then, the ship's resistance, the effective power, the power received by the propeller, and the propulsive efficiency were obtained. At the same brash ice concentration and ice thickness, the propeller rotation speed is closely related to the draft depth of the hull due to the influence of the wet surface area.

(4) Under scantling draft conditions, the maximum errors in the numerical values of the polar transport ships and the predicted values of the ice resistance and total thrust are 10.51% and 2.41%, respectively, and the maximum error of the propulsion efficiency is 15.00%. Under design draft conditions, the maximum errors of the numerical values and the predicted values of the ice resistance and total thrust are 8.39% and 6.29%, respectively, and the maximum error of the propulsion efficiency is 14.06%. The calculation error is within a reasonable range. The functional relationship of the total ice resistance, total thrust, delivered power, and effective power with the brash ice thickness was obtained.

(5) In this study, three empirical formulas were used: the Juve and Riska, Spencer, and DuBrovin formulas. The empirical formula results were compared with the numerical simulation results and test values under different draft and brash ice thickness conditions for polar transport ships. It was found that the numerical simulation results of ice resistance under different draft conditions are in good agreement with the experimental values. Under the scantling draft conditions, the discrepancy between the Spencer formula, DuBrovin formula, and test value was minimal. Under the design draft conditions, the error between the DuBrovin empirical formula and the experimental value was the smallest.

Author Contributions: Conceptualization, J.Z. (Jinlong Zhang) and J.Z. (Jianing Zhang); Methodology, J.Z. (Jinlong Zhang) and L.Z.; Software, J.Z. (Jinlong Zhang); Validation, J.Z. (Jinlong Zhang), J.Z. (Jianing Zhang) and W.C.; Formal analysis, J.Z. (Jinlong Zhang); Investigation, J.Z. (Jinlong Zhang) and Q.Z.; Resources, J.Z. (Jianing Zhang); Data curation, J.Z. (Jinlong Zhang) and Q.Z.; Writing—original draft, J.Z. (Jinlong Zhang); Writing—review & editing, J.Z. (Jinlong Zhang) and J.Z. (Jianing Zhang); Visualization, J.Z. (Jinlong Zhang); Supervision, J.Z. (Jianing Zhang), L.Z. and W.C.; Funding acquisition, J.Z. (Jianing Zhang). All authors have read and agreed to the published version of the manuscript.

Funding: This work was supported by Shanghai Merchant Ship Design & Research Institute (SDARI) in China "Research on optimized polar environmental protection transport ships"; Natural Science Foundation of Liaoning Province (2024-MS-016); the Fundamental Research Funds for the Central Universities of China (3132023123); China COSCO Shipping Corporation Limited "Numerical and Experimental Study of Seakeeping Performance for Ships in High Sea States" (2023-2-Z001-02-01); The model tests in brash ice channels is performed by HSVA, the polar transport ship of 68k MPV vessel is designed by SDARI, to which the authors are most grateful.

Institutional Review Board Statement: Not applicable.

Informed Consent Statement: Not applicable.

Data Availability Statement: Data are contained within the article.

Conflicts of Interest: Authors Weimin Chen and Qingshan Zhang were employed by the company Shanghai Ship and Shipping Research Institute Co., Ltd. The remaining authors declare that the research was conducted in the absence of any commercial or financial relationships that could be construed as a potential conflict of interest.

References

1. Shimanskiĭ, I.U.A. *Conditional Standards of Ice Qualities of a Ship*; Marine Computer Application Corporation: Noida, India, 1969.
2. Kashteljan, V.I. Ice resistance to motion of a ship. *Sudostr. Leningr.* **1968**.
3. Edwards, R.Y., Jr.; Major, R.A.; Kim, J.K.; German, J.G.; Lewis, J.W.; Miller, D.R. *Influence of Major Characteristics of Icebreaker Hulls on Their Powering Requirements and Maneuverability in Ice*; Society of Naval Architects and Marine Engineers: New York, NY, USA, 1976.
4. Zhou, L.; Ling, H.; Chen, L. Model tests of an icebreaking tanker in broken ice. *Int. J. Nav. Archit. Ocean. Eng.* **2019**, *11*, 422–434. [CrossRef]
5. Zong, Z.; Yang, B.Y.; Sun, Z.; Zhang, G.Y. Experimental study of ship resistance in artificial ice floes. *Cold Reg. Sci. Technol.* **2020**, *176*, 103102. [CrossRef]
6. Huang, Y.; Huang, S.; Sun, J. Experiments on navigating resistance of an icebreaker in snow covered level ice. *Cold Reg. Sci. Technol.* **2018**, *152*, 1–14. [CrossRef]
7. *ITTC 7.5-02-04-01*; General Guidance and Introduction to Ice Model Testing. International Towing Tank Committee (ITTC): Zürich, Switzerland, 2017.
8. *ITTC 7.5-02-04-02.1*; Resistance Tests in Ice. International Towing Tank Committee (ITTC): Zürich, Switzerland, 2017.
9. Cundall, P.A.; Strack, O.D.L. A discrete numerical model for granular assemblies. *Geotechnique* **1979**, *1*, 47–65.
10. Vu-Quoc, L.; Zhang, X.; Walton, O.R. A 3-D discrete-element method for dry granular flows of ellipsoidal particles. *Comput. Methods Appl. Mech. Eng.* **2000**, *187*, 483–528. [CrossRef]
11. Løset, S. Discrete element modelling of a broken ice field—Part I: Model development. *Cold Reg. Sci. Technol.* **1994**, *22*, 339–347. [CrossRef]
12. Squire, V.A. Of ocean waves and sea-ice revisited. *Cold Reg. Sci. Technol.* **2007**, *49*, 110–133. [CrossRef]
13. Su, B.; Riska, K.; Moan, T. A numerical method for the prediction of ship performance in level ice. *Cold Reg. Sci. Technol.* **2010**, *60*, 177–188. [CrossRef]
14. Kim, H.S.; Ryu, C.H.; Park, K.D.; Lee, J. Development of estimation system of ice resistance with surface information of hull form. *Ocean. Eng.* **2014**, *92*, 12–19. [CrossRef]
15. Zhang, J.; Zhang, Y.; Shang, Y.; Jin, Q.; Zhang, L. CFD-DEM based full-scale ship-ice interaction research under FSICR ice condition in restricted brash ice channel. *Cold Reg. Sci. Technol.* **2022**, *194*, 103454. [CrossRef]
16. Li, Z.F.; Wu, G.X. Hydrodynamic force on a ship floating on the water surface near a semi-infinite ice sheet. *Phys. Fluids* **2021**, *33*, 127101. [CrossRef]
17. Luo, W.; Jiang, D.; Wu, T.; Guo, C.; Wang, C.; Deng, R.; Dai, S. Numerical simulation of an ice-strengthened bulk carrier in brash ice channel. *Ocean. Eng.* **2020**, *196*, 106830. [CrossRef]
18. Liu, L.; Ji, S. Comparison of sphere-based and dilated-polyhedron-based discrete element methods for the analysis of ship–ice interactions in level ice. *Ocean. Eng.* **2022**, *244*, 110364. [CrossRef]
19. Li, F.; Suominen, M.; Kujala, P. Ship performance in ice channels narrower than ship beam: Model test and numerical investigation. *Ocean. Eng.* **2021**, *240*, 109922. [CrossRef]
20. Islam, M.; Mills, J.; Gash, R.; Pearson, W. A literature survey of broken ice-structure interaction modelling methods for ships and offshore platforms. *Ocean. Eng.* **2021**, *221*, 108527. [CrossRef]
21. Wang, C.; Hu, X.; Tian, T.; Guo, C.; Wang, C. Numerical simulation of ice loads on a ship in broken ice fields using an elastic ice model. *Int. J. Nav. Archit. Ocean Eng.* **2020**, *12*, 414–427. [CrossRef]
22. Kim, J.H.; Kim, Y.; Kim, H.S.; Jeong, S.Y. Numerical simulation of ice impacts on ship hulls in broken ice fields. *Ocean Eng.* **2019**, *182*, 211–221. [CrossRef]
23. Yang, B.; Zhang, G.; Huang, Z.; Sun, Z.; Zong, Z. Numerical simulation of the ice resistance in pack ice conditions. *Int. J. Comput. Methods* **2020**, *17*, 1844005. [CrossRef]
24. Zhang, L.; Wei, Y.; Deng, Y.; Yin, H.; Zhang, Y.; Shang, Y.; Zhang, J. A comparative investigation of fixed and free-running CFD self-propulsion models on a waterjet-propelled trimaran. *Ocean Eng.* **2021**, *232*, 109081. [CrossRef]
25. Zou, M.; Zou, Z.J.; Zou, L.; Chen, C.Z.; Zhang, X.S. Numerical investigations of the ice force distributions on a ship in brash ice channel using a simplified CFD-DEM solving framework. *Ocean Eng.* **2024**, *312*, 119103. [CrossRef]
26. Xie, C.; Zhou, L.; Ding, S.; Liu, R.; Zheng, S. Experimental and numerical investigation on self-propulsion performance of polar merchant ship in brash ice channel. *Ocean Eng.* **2023**, *269*, 113424. [CrossRef]
27. Siemens PLM Software. *Simcenter STAR-CCM+® Documentation*, Version 2019; Siemens PLM Software: Plano, TX, USA, 2019.
28. HSVA. *Brash Ice Tests for 68k MPV with Ice Class 1A, Appendix A Photos*; HSVA: Hamburg, Germany, 2022.
29. Zhang, J.; Zhang, Y.; Shang, Y.; Jin, Q.; Zhang, L. Research on the construction of ship's numeral brash ice field and calculation method of ice resistance. *J. Ship Mech.* **2021**, *25*, 879–890.
30. ITTC. *Recommended Procedures and Guidelines: Uncertainty Analysis in CFD Verification and Validation Methodology and Procedures*; ITTC: Copenhagen, Denmark, 2014.

31. Juva, M.; Riska, K. On the power requirement in the Finnish-Swedish ice class rules. In *Research Report No.53*; Helsinki University of Technology Ship Laboratory: Espoo, Finland, 2002.
32. Spencer, D.; Jones, S.J. Model-scale/full-scale correlation in open water and ice for Canadian Coast Guard "R-Class" icebreakers. *J. Ship Res.* **2001**, *45*, 249–261. [CrossRef]
33. Dubrovin, O.V.; Aleksandrov, M.; Moor, R. *Calculation of Broken Ice Resistance Based on Model Testing*; University of Michigan: Ann Arbor, MI, USA, 1970.

Disclaimer/Publisher's Note: The statements, opinions and data contained in all publications are solely those of the individual author(s) and contributor(s) and not of MDPI and/or the editor(s). MDPI and/or the editor(s) disclaim responsibility for any injury to people or property resulting from any ideas, methods, instructions or products referred to in the content.